SAND2013-3646C

EXPERIMENTAL INVESTIGATION OF NOZZLE ASPECT RATIO EFFECTS ON UNDEREXPANDED HYDROGEN JET RELEASE CHARACTERISTICS

Ruggles, A.J. and Ekoto, I.W.
Sandia National Laboratories, Livermore, CA 94551-0969, USA, ajruggl@sandia.gov

ABSTRACT

Most experimental investigations of underexpanded hydrogen jets have been limited to circular nozzles in an attempt to better understand the fundamental jet-exit flow physics and model this behaviour with pseudo source models. However, realistic compressed storage leak exit geometries are not always expected to be circular. In the present study, jet dispersion characteristics from rectangular slot nozzles with aspect ratios from 2 to 8 were investigated and compared with an equivalent circular nozzle. Schlieren imaging was used to observe the jet-exit shock structure while quantitative Planar Laser Rayleigh Scattering was used to measure downstream dispersion characteristics. These results provide physical insight and much needed model validation data for model development.

1.0 INTRODUCTION

A prerequisite for large-scale hydrogen storage and delivery infrastructure development is the implementation of science based safety codes and standards that are guided by validated engineering models within quantitative risk analysis tools [1]. A key input required for the efficacy of these tools is the release morphology and dominant flow phenomena from unintended hydrogen leaks [2]. Releases are typically assumed to be from circular sources since for fixed mass flow rates these are thought to produce the most conservative (i.e., longest) hazard boundaries used to specify separation distances [3, 4]. Furthermore, a substantial amount of work has been performed to characterize relevant parameters due to axis symmetry, which is amenable to simplified one-dimensional modelling [5-11]. Releases from more realistic cracks and slits, are expected to have shorter flammable extents due to larger ratios of mixing surface area to leak volume. However, for applications where suitable separation distances from hydrogen bulk storage are prohibitive (e.g., releases from on-board storage) there remains a danger that highly flammable mixture could develop close to the release point, which could increase the localized harm potential [12].

Beck et al. [13], has developed analytic methods to model mass flow rates from cracks with varying tortuosity as a function of pressure dissipation from viscous, inertial, and expansion effects. Large pressure losses from thin cracks are likely to result in incompressible planar or slot jets, which Krothapalli et al. [14] noted contain 3 prominent decay regions: the potential core, a two-dimensional region with an inverse half-power centerline decay rate, and the canonical axisymmetric region observed for circular jets with an inverse centerline decay rate. Mi et al. [15] further noted the existence of a transition region between the two-dimension and axisymmetric regions that shrinks as nozzle aspect ratio (AR) increases. For lower AR releases where exit backpressures relative to the ambient are expected to be above the critical ratio (~1.9 for hydrogen), exit flows choke and an underexpanded jet with complex near-field shock structure forms. A Mach disk serves as the boundary between the supersonic and subsonic jet portions, and can be several factors larger than the original release diameter. Notional nozzle models have been developed to predict circular nozzle effective diameters and thermodynamic state variables; the effectiveness of different model formulations for choked hydrogen flows was evaluated experimentally by Ruggles and Ekoto [11] and numerically by Papanikolaou et al. [10]. Beyond the compressible flow region, subsonic integral dispersion models have been used to reconstruct mean scalar and velocity fields [7, 8, 16]. No analogous choked slot source model exists due to a lack of downstream scalar and/or velocity validation data.

Despite the lack of downstream dispersion measurements, there has been limited experimental and numerical research into choked slot nozzle near-field flow features for various gases. Rajakuperan and Ramaswamy [17] observed that the shock structure along the major axis of underexpanded elliptical

air jets resembled that of circular jets, while the classic barrel shock disappeared along the minor axis. Furthermore, "axis switching" occurred for moderate AR (AR > 1.4) where the major axis jet spreading rate reached an asymptote, while the minor axis continued to grow beyond the Prandtl-Meyer expansion; the magnitude of the asymmetry increased with higher backpressures. Similar observations were made from slot air jet simulation and experimental results by Menon and Skews [18] along with simulation results of slot hydrogen jets by Makarov and Molkov [19]. Makarov and Molkov further noted that far-field velocity and scalar fields in the incompressible regime returned to axis-symmetry. For the present study, jet-exit shock structures were imaged via schlieren photography while quantitative Planar Laser Rayleigh Scattering imaging was used to measure downstream dispersion characteristics. These data will serve as validation benchmarks for numerical simulations and for follow-on slot nozzle source and dispersion modelling.

2.0 EXPERIMENTAL DESCRIPTION

To create the desired circular and slot underexpanded hydrogen jets, a high-pressure stagnation chamber with a 1.24 litre internal volume and capable of pressures up to 60 bar was used; a schematic is provided in Figure 1. A uniform stagnation flow field was achieved through the use of a multi-hole injector at the chamber base. Interchangeable nozzles with were machined from flanged blanks that attached to a Swagelok one inch VCO fitting at the chamber outlet. For the circular aperture, a standard ASME long radius nozzle profile with a 1.5 mm outlet diameter was selected due to its relatively top-hat exit profile and large discharge coefficients (CD = 0.979) [20]. Three knife edged rectangular slot nozzles with aspect ratios of 2, 4, and 8 were machined into the flanged VCO blanks. Note that the flow rates for jets with AR of 2 and 8 were found to be identical, while the jet with an AR of 4 was approximately 8% lower. The length and width of each slot nozzle was set such that the exit area was equivalent to that of the 1.5 mm diameter circular nozzle. Schematics of a representative slot and circular nozzle are included in Figure 1. Chamber temperature and pressure were respectively monitored via a type K thermocouple and TESCOM series 100 pressure transducer, with dynamic feedback used to maintain a steady 10:1 pressure ratio. The Abel-Noble equation of state was used to account for compressibility effects in the mass flow rate calculations [6]. Atmospheric laboratory pressure and temperature were 99.673 kPa (±0.17 kPa) and 292 K (±1 K) respectively. The entire assembly was mounted to a computer controlled traverse, with data acquisition and system control handled via custom written LabView program.

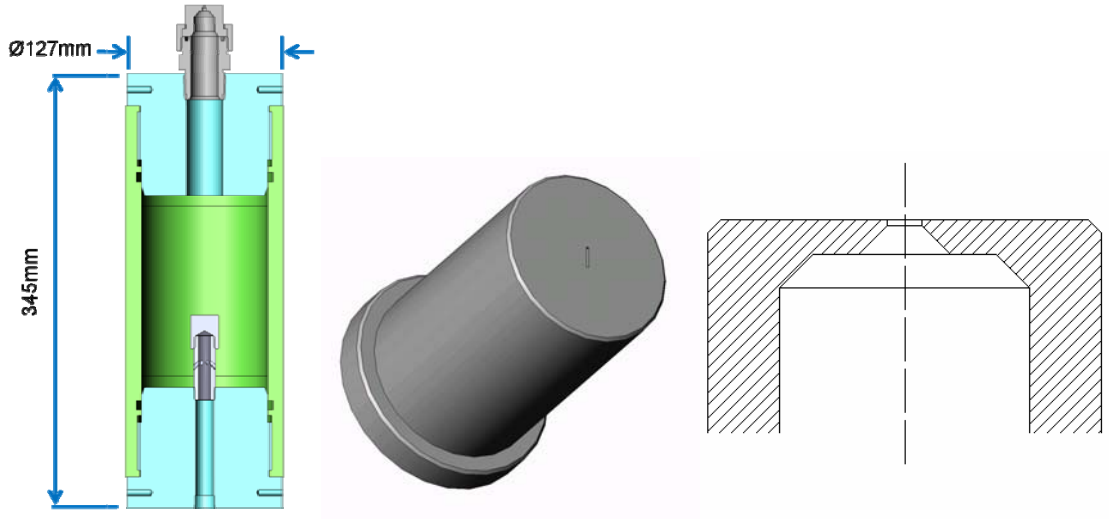

Figure 1. Sectional view of the stagnation chamber and nozzle assembly (left) along with a picture of the nozzle with the AR 8 exit (centre) and a corresponding sectional view (right).

2.1 Schlieren Imaging System

The underexpanded jet shock structure was imaged by an in-line lens based schlieren system, which used a custom light-emitting diode (LED) light source with a fixed 520 nm (green) wavelength to remove chromatic aberrations. The LED was pulsed by a custom driver to achieve pulse durations of 5 μs. The light pulse was focused down by an f/1.2 NIKON 50 mm camera lens with an aperture mounted at the focal point to create a point light source. The schlieren system consisted of three 50.8 mm spherical plano convex lenses: the first (f = 250 mm) was positioned at the focal length to collimate the light, the second (f = 500 mm) focused the collimated light to a point where a horizontally orientated razor blade was positioned to control light cut-off, and a third (f = 350 mm for a global view or f = 150 mm for a close up view) focused the light onto the CCD array of a Princeton Instruments PIXIS 400B camera. Each recorded image was subsequently corrected for electronic bias, E_B, spurious background luminosity, B_G, and lens system optical response, O_R.

$$I = \frac{R - E_B - B_G}{O_R} \tag{1}$$

2.2 Planar Laser Rayleigh Scatter (PLRS) Imaging System

Planar Laser Rayleigh Scatter (PLRS) imaging was used to measure instantaneous mole fractions within the isothermal portion of the jet. This region was defined by temperatures being within 2° C of ambient, which limited the associated bias error for pure hydrogen to 0.4%. A Nd:YAG laser beam (9 ns pulse, 1 J/pulse, 532 nm wavelength) was formed into an ~40 mm high laser sheet using a cylindrical plano-concave (f = -200 mm) and spherical plano-convex (f = 1000 mm) lens pair. Starting 50 mm downstream of the jet exit, 400 images were recorded, with the imaging area successively moved downstream in 30 mm increments until 250 mm of the release point. To limit unwanted scatter, the laser and sheet forming optics were encased within a light tight enclosure. Once the laser sheet passed through the test section, the light was directed into a secondary enclosure with a built-in beam dump to minimize back scatter. A Princeton Instruments PIXIS 400B camera mounted perpendicular to the laser sheet and equipped with an f1.2 NIKON 50 mm lens with a NIKON 3T close up lens was used to image the Rayleigh scattered light. A detailed illustration of the PLRS system is provided in Figure 2.

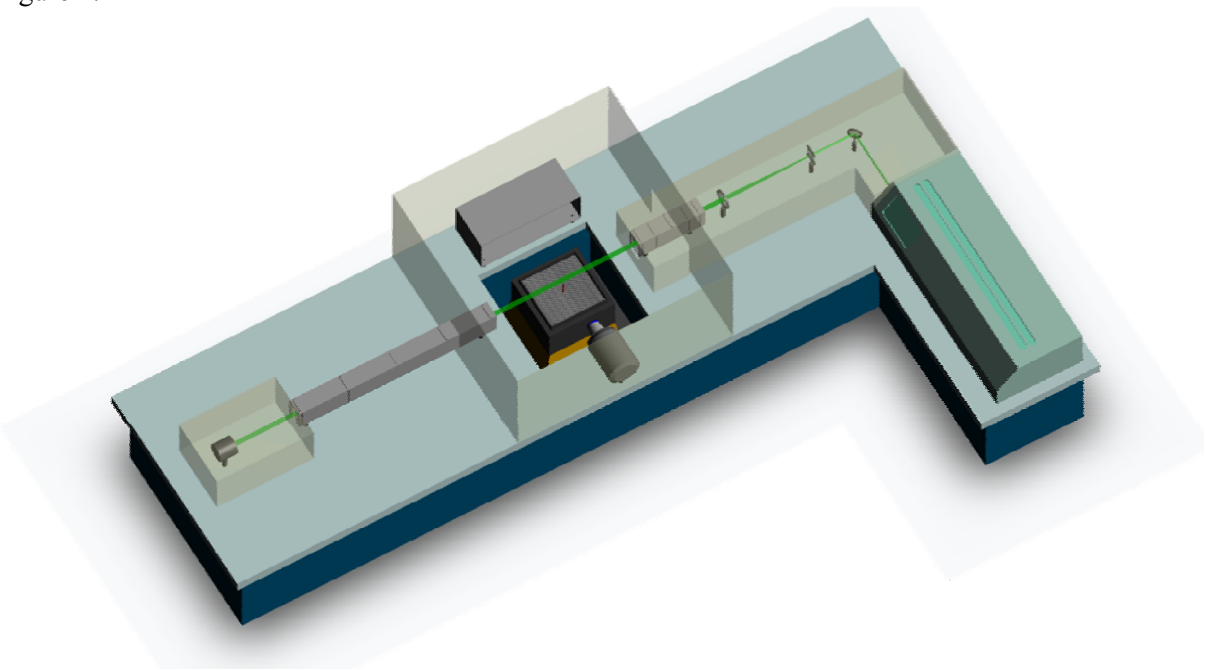

Figure 2. Detailed illustration of the planar Rayleigh laser scatter setup.

To improve signal-to-noise (SNR), 2×2 on chip binning and 3×3 Gaussian smoothing was used. The system was calibrated from separate ensemble images (800) of pure air and helium streams. Image intensity, I, was a function of the scattering background, S_B, camera optical response, O_R, electronic bias, E_B, background scatter, B_G, laser power fluctuations, p_F, and laser sheet intensity variations, S_t.

$$I = \frac{1}{St} \cdot \left[\left(\frac{R - E_B - B_G}{p_F \cdot O_R} \right) - S_B \right] \tag{2}$$

Raw images were subjected to a custom post-processing dust filter. A conservative estimate for single-shot measurement uncertainty was ±0.6% (mole fraction) for a 95.4% confidence interval. Mole fractions were calculated from the corrected signal intensity and the calibrated intensity values for pure air and hydrogen:

$$\chi_{H_2} = \frac{I_{AIR} - I}{I_{AIR} - I_{H_2}} \tag{3}$$

Concentration data were expressed in terms of mass fraction, Y_{H2}, from the known hydrogen and air molar masses to account for momentum differences due to density effects [21]. Statistical uncertainties were quantified using the Jackknife re-sampling technique. Further details about the imaging diagnostics and statistical uncertainty can be found in Ruggles and Ekoto [11].

3.0 SCHLIEREN IMAGING

Mean corrected near- and far-field schlieren images for all nozzles examined are presented in Figure 3, with both the major and minor axes displayed for the slot nozzles. For the circular nozzle, the classical barrel shock, Mach disk, and outer compression waves were observed. The Mach disk diameter measured 1.30 mm and located 3.05 mm downstream from the nozzle exit. Downstream of the Mach disk, characteristic diamond shaped reflected shock structures were likewise present.

For the slot nozzles, schlieren image shock structure was qualitatively similar to previous observations for air slot nozzle [17, 18]. In particular, the axis switching phenomena was observed, where the radial portion of the compressible jet boundary approached an asymptote along the major axis while linearly expanding along the minor axis. Along the major axis, the slip region formed by expansion fans at the outer jet boundary appeared to have larger initial spreading ratios than was observed for similar underexpanded slot air jets, possibly due to non-ideal gas compressibility effects of the injected hydrogen gas [17]. Within the jet core, turnip shaped barrel shocks were observed where higher aspect ratios led to increasingly convergent incident shocks. These shocks underwent an irregular reflection forming a Mach stem. This feature extends further downstream with increasing aspect ratio, before being reflected back towards the slip region. The Mach stem appears to extend further downstream for increasing aspect ratios for the same pressure ratio. The incident shock was not observed along the minor axis. The downstream oblique shock train was increasingly convergent towards the centreline relative to the major axis dimension as the aspect ratio increased, with the shock structure disappearing at roughly the same downstream axial distance (~12 – 17 mm).

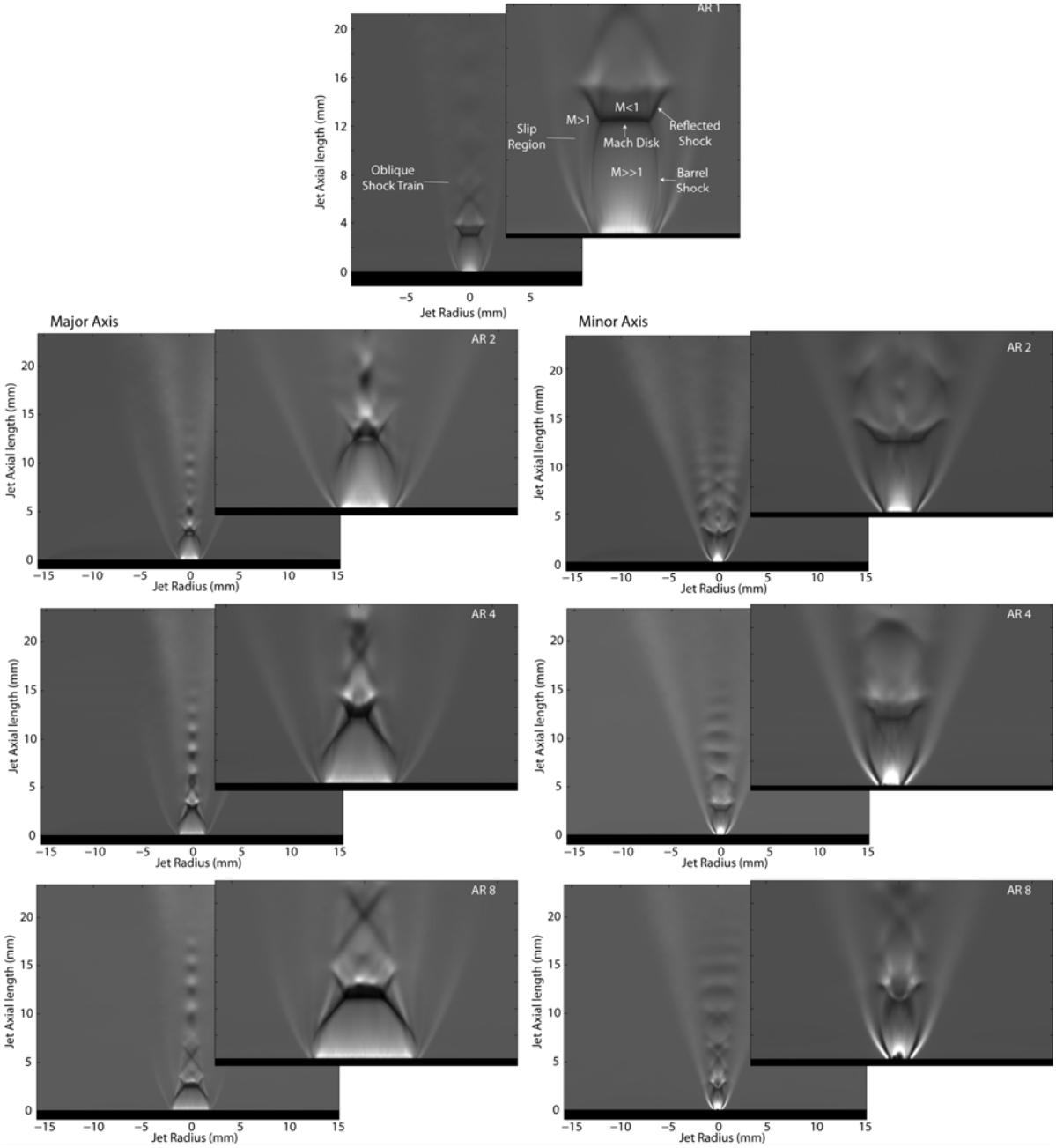

Figure 3. Mean schlieren images of the underexpanded jet and downstream shock structure for the circular aperture (top), along with all slot jet major (left column) and minor axes (right column).

4.0 SCALAR CONCENTRATION RESULTS

Images of the mean mass fraction fields for the axisymmetric jet (AR = 1) from Ruggles and Ekoto [11] along with a slot jet along the major and minor axes (AR = 8) from the current measurements are displayed in Figure 4. These images illustrate the nearly seamless sectional reconstruction of the concentration fields. Qualitatively, it is evident that elevated mean mass fraction contours extend further downstream for the axisymmetric jet, which is due in part to the higher overall discharge coefficient for this jet. For the slot jet major axis, the radial extent was very narrow in the near-field relative to the minor axis. However, jet spreading rates appear to be faster along the major axis and the concentration field approach axis-symmetry at the furthest downstream recorded location.

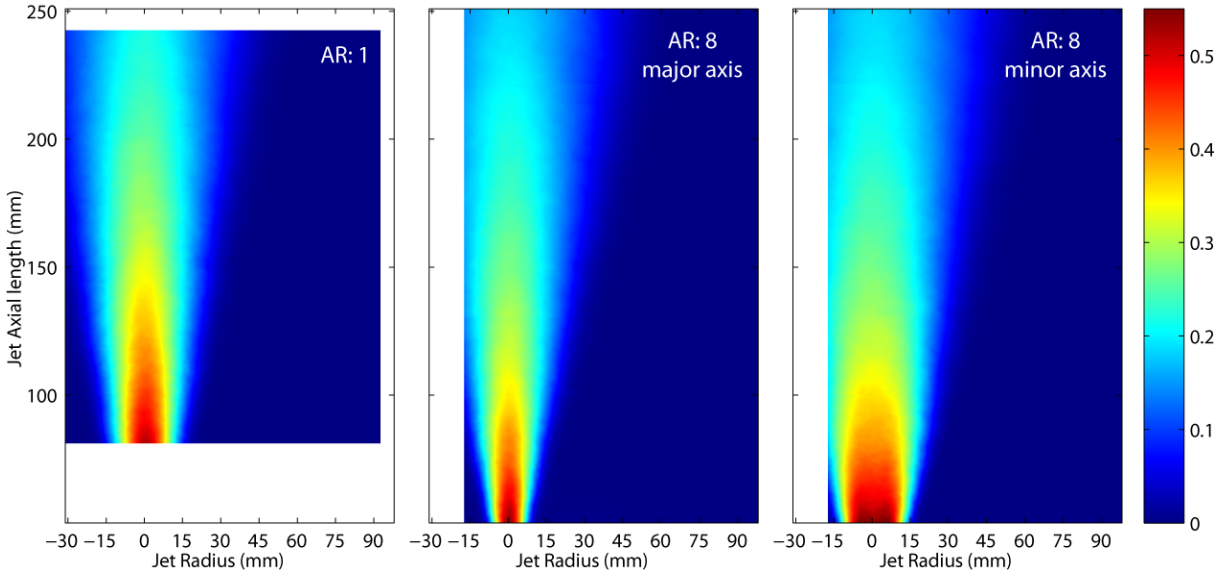

Figure 4. Mean mass fraction contour plots for the circular nozzle (left) along with the AR 8 major (centre) and minor axes (right). Data contours from the circular nozzle are cropped below 80 mm since scalar measurements were not acquired in this region.

Inverse mass fraction profiles along the centreline are plotted in Figure 5 against the downstream location normalized by the effective jet-exit radius ($r_0 = 0.75$mm). Note that the profile for the AR 4 jet was corrected for the previously noted lower flow rate. With this correction, all slot nozzle decay profiles converge towards a uniform curve; it remains to be seen if this trend holds for higher pressure or aspect ratios. As expected, the initial decay rates for the slot jets was much faster than for the corresponding circular nozzle, in part due to the lower discharge coefficient (and hence mass flow rate), but also due to improved mixing along the larger effective jet surface area. The decay rates were linear at most downstream locations, although there appears to be a slight non-linear growth rate for the slot jets in the near field. It is not expected that this is the trailing edge of the two dimensional region described by Krothapalli et al. [14], as the decay rate steepens relative to the downstream linear region. Instead it is thought that temperature effects due to slightly cooler temperatures have biased the results. The affect is small, however and does not impact the analysis.

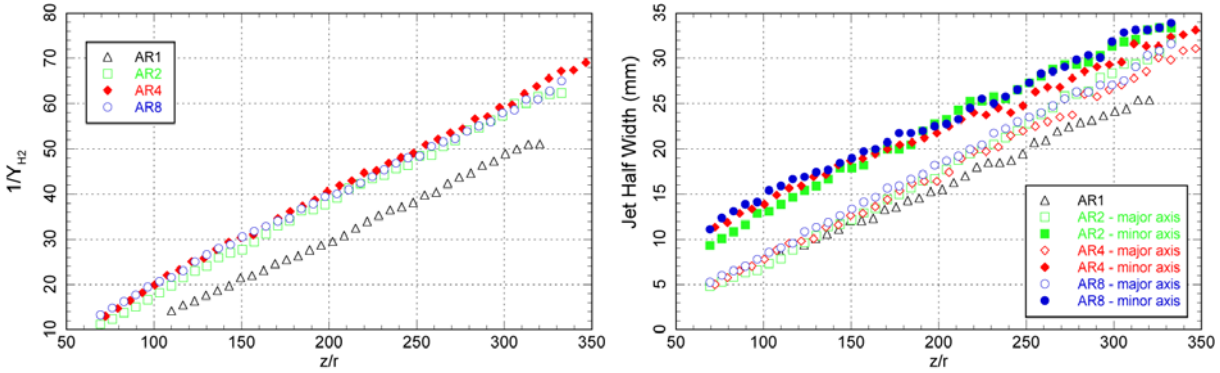

Figure 5. Left: Reciprocal mean mass fraction along the centreline with Jackknife uncertainties. Right: Jet half widths against normalized axial distance.

Also displayed in Figure 5 are the jet half widths, defined as the full width at half maximum for the mean concentration radial profiles at each axial location, along both the minor and major axes for all jets. As expected, the jet half widths along the major axis are initially much smaller than the corresponding half widths along the minor axis, due to the axis switching phenomena that accelerated the jet spreading rates along the minor axis. Moving downstream it is clear that the spreading rates for

both axes are approaching convergence. This is true for all aspect ratios. The point where each jet achieves axis-symmetry was just outside of the interrogation region for the present jet, and is difficult to extrapolate as the growth rates are slightly non-linear. Once convergence does occur it is unknown if one of the axes will change its growth of jet spreading rate to match the other, or if both will change to match a value more typical of axisymmetric jets.

It remains an open question as to when and where the jets return to self-similarity, and whether some sort of axes specific non-dimensional scaling could be used to enable 1-D integral models (e.g., [7, 8]) to specify jet and plume characteristics for these choked slot release types. To shed some light on this question, the radial mean mass fraction profiles were plotted at select axial locations and plotted against the normalized radial coordinate, η ($\eta = r/z$).

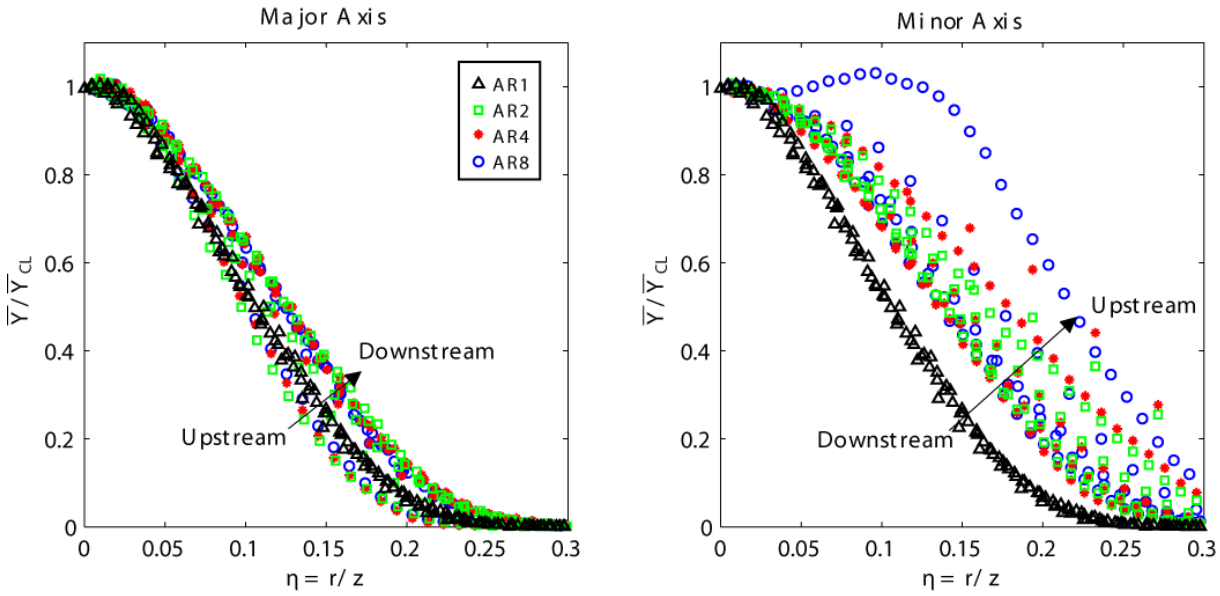

Figure 6. Radial mean mass fraction profiles in the major (left) and minor (right) axes planes for the circular nozzle and the three examined slot jets plotted against the non-dimensional radial coordinate, η. Profiles were extracted at z/r_0 = 69, 137, 204, 271 and 322 where r_0 = 0.75mm.

The radial profiles for the circular nozzle clearly collapse to a common curve as expected. The profiles for the major axis of the rectangular nozzles are reasonably similar to the those of the circular nozzle. However none of the profiles of any rectangular nozzle collapse to a respective common curve, or collapse to that of the circular nozzle. Common behaviour amongst the rectangluar nozzles is that the more upstream profiles lie beneath the circular nozzle profile. Moving downstrream the radial profiles become larger than that of the circular nozzle profile. Considering the minor axis all of the profiles for all three reactangular nozzles lie above the circular nozzle profile. The axial behaviour of the minor axis profiles is the opposite of the major axis profiles, the downstream profiles are closer to that of the circular nozzle. Additionally there is considerable difference in behaviour amongst the retangular nozzles, particulalry AR 8 where the upsream profile has a maximum away from the centreline. This can be discerned from Figure 4. This marks a clear depature away from Gaussian behaviour within the upstream part of the jet.

In Figure 7 the same profiles have been plotted against the normalized radial coordinate, η ($\eta = r/(z-C_m)$). For circular nozzles the constant C_m is the momentum virtual origin. For the rectangular nozzles C_m has been calculated in the same way for each axis but is not referred to as a virtual origin as self similarity has not been established. In addition the curve fit for self similar axisymmetric jets of Richard and Pitts is also plotted [22].

The major axis profiles of each nozzle collapse well to respective common curves. However none collapse to the Richards and Pitts curve and all lie above it with the smaller aspect ratio nozzle furthest away. For the minor axis a significant improvement in collapse is observed over the corresponding profiles in Figure 6. Profiles of AR 2 are clearly above Richards and Pitts. Profiles of AR 4 show better agreement until $\eta \approx 0.17$ where the profiles fall below the Richards and Pitts curve. The majority of the profiles for AR 8 agree reasonably well with Richards and Pitts. However the upstream profile does not collapse as clearly shown. This is due to the non-Gaussian behavior of the mean scalar field in the upstream locations of the field of view imaged.

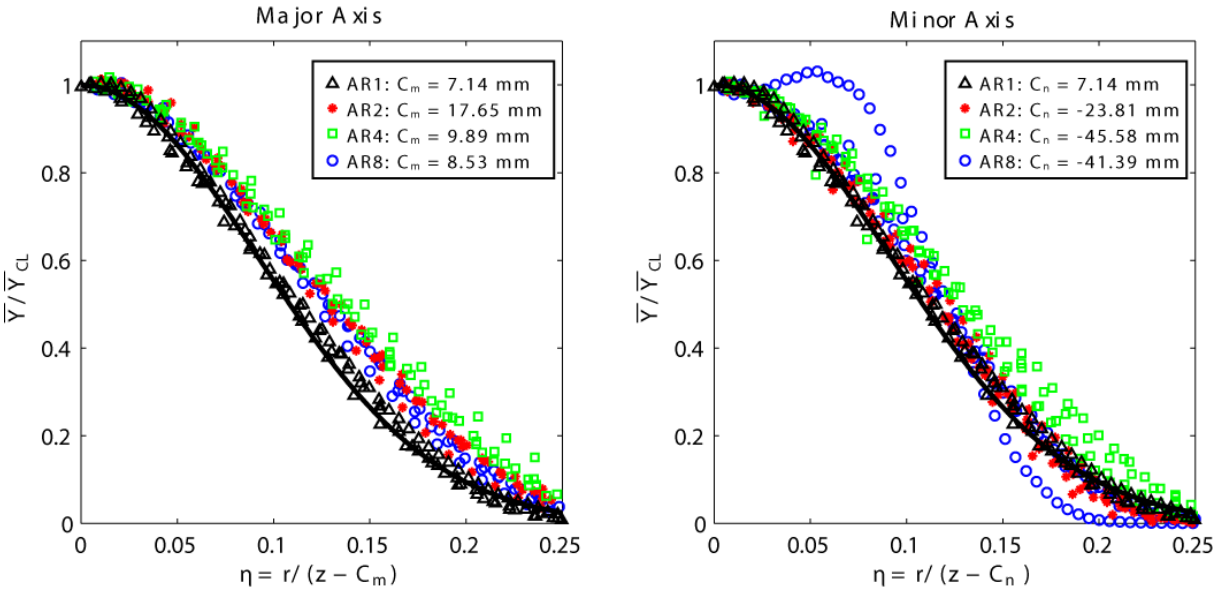

Figure 7. Radial mean mass fraction profiles in the major (left) and minor (right) axes planes for the circular nozzle and the three examined slot jets plotted against the non-dimensional radial coordinate, η, where the momentum origin term described above was used to collapse each profile to a common curve. The empirical Gaussian curve fit from Richards and Pitts [22] is likewise plotted. Profiles were extracted at $z/r_0 = 69$, 137, 204, 271 and 322 where $r_0 = 0.75$mm.

5.0 CONCLUSIONS AND FUTURE WORK

Underexpanded jets of pressure ratio 10 issuing from rectangular shaped nozzles of aspect ratios 2, 4, and 8 have been compared to an under expanded jet issuing from a 1.5mm diameter circular nozzle. Schlieren imaging has been used to characterize the shock structures and has shown the axis switching behavior occurring that is responsible for differences in jet growth rates for the two axes. Additionally the Schlieren imaging revealed shock structures unique to each axis. Quantitative Planar Laser Rayleigh Scatter was used to determine the mean scalar fields of both major and minor axes. Using this data it was shown the centerline inverse mass fraction decay profiles collapsed to a common profile. Jet half width profiles showed that for each axis the profiles from the different rectangular nozzles were broadly similar and the profiles of major and minor axes are approaching convergence. Radial profiles of the mean scalar fields require a momentum constant in order to achieve even a modest collapse which in most cases does not agree with the empirical Gaussian curve established by Richards and Pitts. Additionally the largest aspect ratio in this study, AR 8, exhibits highly non-Gaussian profiles in the upstream region of the flow investigated.

Further work needs to be undertaken to address if the departure from Gaussian shaped radial profiles continues with larger aspect ratios. The positions where the jet half width profiles converge need to be identified and determined if they can be simply predicted. Additionally the jet half width behavior after the convergence point needs to be ascertained and whether the scalar field is truly self similar from this point onwards. Assuming this is true the question whether the region upstream can be

described by a modified self similar argument specific to each axis needs to be addressed. This is necessary as this pre-axisymmetric region is likely to be large and non-trivial when considering large scale leaks from highly pressurized devices. Additionally the correct prediction of this region will be necessary before the application of axisymmetric self similarity for the majority of the downstream aspect of the jet.

6.0 ACKNOWLEDGMENTS

This research was supported by the United States Department of Energy Fuel Cell Technologies Office, under the Safety, Codes, and Standards subprogram element managed by Will James. Sandia is operated by the Sandia Corporation, a Lockheed Martin Company, for the U.S. DOE under contract No. DE-AC04-94-AL8500.

7.0 REFERENCES

[1] LaChance J, Tchouvelev A, Ohi J, Risk-informed process and tools for permitting hydrogen fueling stations. Int J Hydrogen Energy, 2009;34:5855-61.

[2] Schefer RW, Houf WG, San Marchi C, Chernicoff WP, Englom L, Characterization of leaks from compressed hydrogen dispensing systems and related components. Int J Hydrogen Energy, 2006;31:1247-60.

[3] LaChance J, Houf W, Middleton B, Fluer L, Analyses to Support Development of Risk-Informed Separation Distances for Hydrogen Codes and Standards. SAND 2009-0874, Sandia National Laboratories, March, 2009.

[4] LaChance JL, Middleton B, Groth KM, Comparison of NFPA and ISO approaches for evaluating separation distances. Int J Hydrogen Energy, 2012;37:17488-96.

[5] Molina A, Schefer RW, Houf WG, Radiative fraction and optical thickness in large-scale hydrogen-jet fires. P Combust Inst, 2007;31:2565-72.

[6] Schefer RW, Houf WG, Williams TC, Bourne B, Colton J, Characterization of high-pressure, underexpanded hydrogen-jet flames. Int J Hydrogen Energy, 2007;32:2081-93.

[7] Houf W, Schefer R, Analytical and experimental investigation of small-scale unintended releases of hydrogen. Int J Hydrogen Energy, 2008;33:1435-44.

[8] Xiao JJ, Travis JR, Breitung W, Non-Boussinesq Integral Model for Horizontal Turbulent Strongly Buoyant Plane Jets. Icone16: Proceeding of the 16th International Conference on Nuclear Engineering - 2008, Vol 3, 2008:225-32.

[9] Xiao J, Travis JR, Breitung W, Hydrogen release from a high pressure gaseous hydrogen reservoir in case of a small leak. Int J Hydrogen Energy, 2011;36:2545-54.

[10] Papanikolaou E, Baraldi D, Kuznetsov M, Venetsanos A, Evaluation of notional nozzle approaches for CFD simulations of free-shear under-expanded hydrogen jets. Int J Hydrogen Energy, 2012;37:18563-74.

[11] Ruggles AJ, Ekoto IW, Ignitability and mixing of underexpanded hydrogen jets. Int J Hydrogen Energy, 2012;37:17549-60.

[12] LaChance J, Tchouvelev A, Engebo A, Development of uniform harm criteria for use in quantitative risk analysis of the hydrogen infrastructure. Int J Hydrogen Energy, 2011;36:59-66.

[13] Beck SBM, Bagshaw NM, Yates JR, Explicit equations for leak rates through narrow cracks. Int J Pres Ves Pip, 2005;82:565-70.

[14] Krothapalli A, Baganoff D, Karamcheti K, On the Mixing of a Rectangular Jet. J Fluid Mech, 1981;107:201-20.

[15] Mi J, Deo RC, Nathan GJ, Characterization of turbulent jets from high-aspect-ratio rectangular nozzles. Phys Fluids, 2005;17.

[16] Jirka GH, Integral model for turbulent buoyant jets in unbounded stratified flows. Part I: Single round jet. Environ Fluid Mech, 2004;4:1-56.

[17] Rajakuperan E, Ramaswamy MA, An experimental investigation of underexpanded jets from oval sonic nozzles. Exp Fluids, 1998;24:291-9.

[18] Menon N, Skews BW, Shock wave configurations and flow structures in non-axisymmetric underexpanded sonic jets. Shock Waves, 2010;20:175-90.
[19] Makarov D, Molkov V, Structure and Concentration Decay in Supercritical Plane Hydrogen Jet. Proc Eight International Symposium on Hazards, Prevention, and Mitigation of Industrial Explosions, Yokohama, Japan, ISH073, September 5-10, 2010.
[20] Measurement of Fluid Flow in Pipes Using Orifice Nozzle and Venturi. ASME MFC-3M-2004 ed.
[21] Pitts WM, Kashiwagi T, The Application of Laser-Induced Rayleigh Light-Scattering to the Study of Turbulent Mixing. J Fluid Mech, 1984;141:391-429.
[22] Richards CD, Pitts WM, Global Density Effects on the Self-Preservation Behavior of Turbulent Free Jets. J Fluid Mech, 1993;254:417-35.